LSTM-Assisted SINS/2D-LDV Tightly Coupled Integration Approach Using Local Outlier Factor and Adaptive Filter

Zhiyi Xiang, Qi Wang, Xiaoming Nie, Shilong Jin, and Jian Zhou

Abstract— The tightly coupled integration of strapdown inertial navigation system (SINS) and 2-D laser Doppler velocimeter (2D-LDV) enhances system robustness by directly using raw 2D-LDV measurements, making it well-suited for land autonomous navigation. However, this approach struggles with long-term failures of individual or both 2D-LDV beams and is sensitive to violations of the vehicle's lateral zero-velocity constraint, which can degrade performance. To address these limitations, this article proposes a novel approach involving a long short-term memory (LSTM)-assisted SINS/2D-LDV tightly coupled integration, incorporating a local outlier factor (LOF) and an adaptive filter. The LOF is introduced to evaluate the anomaly degree of the system's measurements, while offline datasets constructed and classified from historical normal data improve detection accuracy and reduce computational load. The LSTM is used to predict the 2D-LDV measurements and the vehicle's lateral velocity, substituting these predictions for anomalous data to mitigate their impact. Furthermore, an adaptive filter is used to adjust the measurement noise covariance matrix of the navigation filter to avoid the adverse effects of potential errors in LSTM predictions. The effectiveness of the proposed method is validated through two groups of experiments, demonstrating satisfactory performance under both normal conditions and prolonged single- or dual-beam failures in the 2D-LDV.

Index Terms— Adaptive filter, land autonomous navigation, local outlier factor (LOF), long short-term memory (LSTM) network, strapdown inertial navigation system (SINS)/2-D laser Doppler velocimeter (SINS/2D-LDV) tightly coupled system.

I. INTRODUCTION

WITH the increasing number of land vehicles, autonomous navigation for land vehicles has emerged as a prominent research focus in the navigation field in recent years. Given the ability of global navigation satellite systems (GNSSs) to provide users with continuous, high-precision positioning information globally, and the decreasing cost of GNSS positioning terminals, the GNSS has been widely used in autonomous vehicle navigation. Nonetheless, GNSS reliability is compromised in challenging environments such as urban canyons, forests, and tunnels, where signals are obstructed [1], [2]. While the strapdown inertial navigation system (SINS) can compensate for GNSS outages, its inherent drawback of cumulative errors over time limits its effectiveness during prolonged GNSS signal loss [3], [4]. Thus, achieving long-term, high-precision autonomous vehicle navigation without the GNSS is a critical challenge, particularly in military and other security-sensitive domains.

Odometers (ODs), cameras, and LiDAR are the most commonly used sensors in autonomous navigation systems for land vehicles except the GNSS [5], [6], [7], [8], [9], [10]. The OD autonomously provides vehicle velocity and distance by gauging the angle of wheel rotation. Their small size, lightweight nature, ease of implementation, and affordability have led to their widespread adoption in land vehicles. However, the precision of OD measurements is compromised by wheel conditions (such as tire pressure and wear) and vehicle operating conditions (including slipping and bumps), leading to reduced accuracy in practical applications. Cameras and LiDAR can capture detailed environmental features and provide navigation data for vehicles through feature tracking and matching. However, factors such as weather conditions, vehicle velocity, and the surrounding environment can impact the reliability of cameras and LiDAR [11], [12].

Laser Doppler velocimeter (LDV) is an optical velocity sensor that employs laser light to measure velocity using the optical Doppler effect. Its application extends across meteorology, biomedicine, fluid dynamics, aerospace, and various other fields, earning acclaim for its precision. Recently, LDV has gained traction in autonomous land vehicle navigation, determining vehicular velocity relative to the ground by measuring the Doppler shift of the scattered light from the outgoing beam [13]. In contrast to OD, LDV has superior velocity measurement accuracy, and its noncontact measurement characteristic renders the velocity measurement value of LDV independent of wheel conditions and less affected by vehicle driving conditions. Furthermore, when compared to cameras and LiDAR, LDV not only achieves higher measurement accuracy but also demands fewer computing resources, exhibits greater adaptability to environmental conditions, and proves more reliable and practical in challenging operational scenarios. Current research demonstrates the effectiveness and superiority of SINS/LDV integration [14], [15], [16], [17], [18].

Currently, SINS/LDV integrated navigation systems primarily use 1-D LDV (1D-LDV), which measures the vehicle's forward velocity along its trajectory [19]. Consequently, 3-D velocity measurement is typically realized using nonholonomic constraints (NHCs). NHC, based on kinematic principles, assumes negligible slip and jump of the vehicle during motion, with lateral and vertical velocities approaching zero. Nonetheless, perfect NHC is impractical due to the inevitable sideslip and vertical motion of the vehicle during maneuvers over uneven terrain, during turns, and under high-speed conditions [20]. Violations of the vertical zero-velocity constraint in NHC complicate the accurate estimation of the pitch installation misalignment angle in SINS/1D-LDV integration, thereby hindering precise height estimation. To address this issue, To address this issue, our previous research improved the optical path structure and modeling method of the traditional LDV, developing a 2-D LDV (2D-LDV) capable of simultaneously measuring the forward and vertical velocities of land vehicles [21], [22], [23]. This innovation eliminates the need for the vertical zero-velocity constraint of NHC, significantly enhancing height estimation accuracy in SINS/2D-LDV integration compared to SINS/1D-LDV integration [23]. Currently, SINS/2D-LDV integration is implemented in two main configurations: loosely coupled and tightly coupled integration. In the loosely coupled configuration, the observation equation is based on the lateral zero-velocity constraint of the NHC and the 2-D velocity synthesized from the two beam velocities of the 2D-LDV. In contrast, the tightly coupled configuration uses the individual beam velocities of the 2D-LDV and the lateral zero-velocity constraint of the NHC to formulate the observation equation. The tightly coupled integration method is more robust than the loosely coupled approach, as it can partially restrict SINS velocity errors by using partial beam measurements of 2D-LDV.

However, since the 2D-LDV cannot measure the vehicle's lateral velocity, the SINS/2D-LDV tightly coupled integration must still rely on the lateral zero-velocity constraint of the NHC. Consequently, any violation of this lateral velocity constraint inevitably impacts the performance of the SINS/2D-LDV tightly coupled integration. Existing studies suggest that configuring NHC parameters necessitates considering the vehicle's motion state, as well as the installation position and angle of the inertial measurement unit (IMU) [24]. Hence, obtaining optimal NHC parameters in practical applications is a complex challenge, and relying solely on manual adjustments often fails to yield ideal results. To address these challenges, Liu et al. explored the correlation between NHC noise and vehicle motion, linked the NHC noise to the vehicle's forward velocity and heading angular velocity, and devised an adaptive NHC noise method based on the vehicle's motion state [25]. Brossard et al. [26] pioneered the application of a deep learning (DL) method based on convolutional neural networks (CNNs), enabling the mapping between the IMU output and NHC observation variance, thus improving the positioning accuracy of IMU dead reckoning. Zhang et al. [24] employed multiple regression and CNNs to directly estimate lateral and vertical vehicle velocities, yielding a substantial accuracy enhancement over traditional NHC noise adjustment methods

in the absence of GNSS. Li et al. [27] in their CNN-based predictions of NHC values, factored in vehicle motion states, enhancing prediction accuracy during maneuvers such as turns. Xu et al. [28] used a back-propagation (BP) neural network to associate vehicle forward velocity, heading angular velocity, and lateral velocity. These studies demonstrate that adaptive adjustments to NHC, whether in the variance or observation domain, improve the positioning accuracy of the integrated navigation system, particularly for high-speed maneuvering vehicles.

In addition to the violation of the NHC lateral zero-velocity constraint, another challenge that the SINS/2D-LDV tightly coupled integration may face in practical applications is the 2D-LDV measurement outliers. The performance of LDV is closely related to the scattered light signal received by the internal detector, which is influenced by ground conditions, lens cleanliness, the distance of the detector to the scattering point, and the operational state of the laser. Although advancements in vehicle-mounted LDV technology generally ensure reliable signal quality, extreme conditions such as water-logged roads and deep potholes present significant challenges. While SINS/2D-LDV tightly coupled integration can partially mitigate speed errors in SINS using partial beam measurements from the 2D-LDV, it struggles to handle simultaneous anomalies in both beams, and prolonged reliance on a single beam significantly degrades system accuracy. Although robust filters (such as the Sage–Husa adaptive filter, strong tracking filter, and maximum correlation entropy-based Kalman filter) and more robust filter observations (such as displacement increment and position information) can effectively mitigate the impact of sensor outliers, they remain inadequate for addressing prolonged sensor failure [29], [30], [31], [32]. In recent years, with the development of artificial intelligence, machine learning, and DL methods have been used to deal with outliers and interrupts of sensors. Techniques such as support vector machines, CNNs, and long short-term memory (LSTM)-based recurrent neural networks have been employed to address output interruptions of GNSS and Doppler velocity log, yielding satisfactory outcomes [33], [34], [35], [36], [37].

Based on the above discussion, 2D-LDV outliers and violations of the NHC lateral zero-velocity constraint are the two primary factors affecting the performance of SINS/2D-LDV tightly coupled integration. To enhance the accuracy and robustness of SINS/2D-LDV tightly coupled integration for various complex applications, it is essential to accurately identify these adverse factors and mitigate their negative effects during system operation. To this end, this article proposes an LSTM-assisted SINS/2D-LDV tightly coupled integration method, which incorporates a local outlier factor (LOF) and an adaptive Kalman filter. The framework of the proposed approach is depicted in Fig. 1, and the principal contributions of this study are delineated as follows.

1) A novel SINS/2D-LDV tightly coupled integrated navigation method is designed, which integrates an SINS/2D-LDV tightly coupled model, LOF, LSTM network, and adaptive filter, which can deal with the lateral constraint violation of vehicle NHC as well as short- and long-term LDV anomalies.
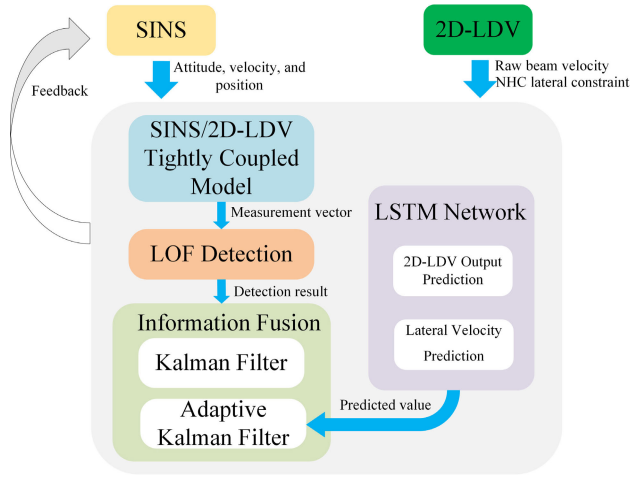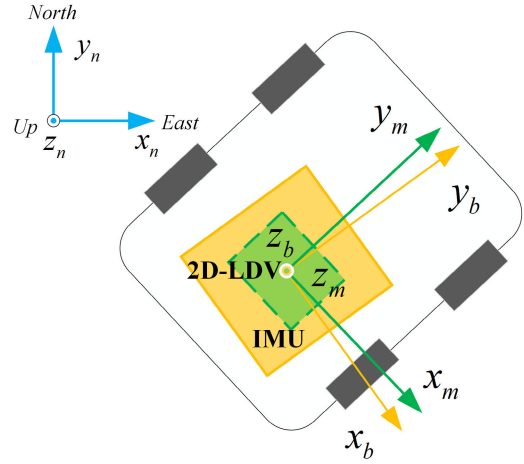
Fig. 1.   Framework of the proposed method.

Fig. 2.   Coordinate system definition.

2) The LSTM model is designed to predict the 2D-LDV outputs and the vehicle lateral velocity. When outliers appear in the integrated navigation system, the predicted values from the LSTM network replace them, reducing their impact on the integrated navigation system.

3) An outlier detection scheme without any specific distributional assumptions is constructed by introducing the LOF and preconstructing and classifying the historical dataset required for detection. This scheme can effectively detect the outlier values of 2D-LDV and the lateral constraint violation of vehicle NHC, providing new insights into fault detection in the SINS/LDV integrated navigation system.

4) An adaptive filter is designed to mitigate the influence of LSTM network predicted value error on the integrated navigation system, thereby improving the accuracy and stability of the system, especially during prolonged use of LSTM network predicted value.

The subsequent sections of this article are structured as follows: Section II introduces the SINS/2D-LDV integrated navigation method. Section III proposes the measurement value prediction scheme based on the LSTM network, presents the structure of the LSTM network, and analyzes the input and output required for 2D-LDV measurement value and vehicle lateral velocity prediction using the LSTM network. Section IV describes the LOF-based fault detection method and the adaptive filter. Section V presents the results and analysis of the vehicle-mounted experiments. Section VI provides the conclusions of this article.

II. REVIEW OF SINS/2D-LDV TIGHTLY COUPLED METHOD

The typical equipment installation relationship for vehicle-mounted SINS/2D-LDV tightly coupled integration is illustrated in Fig. 2. The navigation-grade IMU is installed at the midpoint of the rear nonsteering axle of the vehicle, with its body frame defined as the b frame. The origin of the b frame is at the IMU's sensitive center, with its three axes x_b, y_b, and z_b, pointing to the right, forward, and upward, respectively. The 2D-LDV is mounted close to the IMU to minimize the

impact of the lever arm on the system. The 2D-LDV's body frame is defined as the m frame, with its origin at the 2D-LDV's measurement center, and its three axes, x_m, y_m, and z_m, pointing to the right, forward, and upward, respectively. The navigation frame adopts the local geographic reference frame, denoted as the n frame, with its axes pointing east, north, and up.

The integration architectures of SINS/2D-LDV are currently classified into two configurations: loosely coupled and tightly coupled. In the loosely coupled architecture, the forward and vertical velocities in the m frame, transformed from the 2D-LDV beam measurements, are integrated with NHC to correct SINS errors. However, the presence of outliers in the 2D-LDV outputs impedes the effective compensation of SINS errors, resulting in the degradation of the SINS/2D-LDV loosely coupled system to a pure inertial navigation system. Conversely, the tightly coupled architecture directly uses the measurement values of each 2D-LDV beam to constrain SINS errors. Even if one beam's measurement is abnormal, the measurement values of the remaining normal beams can still effectively mitigate SINS errors, thereby enhancing system robustness [22].

A. State Equation Model

The SINS/2D-LDV integrated navigation system typically undergoes precise calibration before utilization, thus this article excludes consideration of the installation misalignment angle error between the IMU and the LDV, as well as the LDV beam inclination error. Detailed discussions of these errors are addressed in [23]. The 15-D error state vector of the SINS/2D-LDV tightly coupled system is described as

$$\boldsymbol{x}_k = \left[\ \boldsymbol{\phi}_n^T \quad \left(\delta \boldsymbol{v}_{\text{SINS}}^n\right)^T \quad \delta \boldsymbol{p}_{\text{SINS}}^T \quad \left(\boldsymbol{\varepsilon}_{ib}^b\right)^T \quad \left(\boldsymbol{\nabla}_{ib}^b\right)^T \ \right]^T \quad (1)$$

where $\boldsymbol{\phi}_n$ represents the attitude error of the SINS. $\delta \boldsymbol{v}_{\text{SINS}}^n$ denotes the SINS's velocity error, with its east, north, and upward components being δv_E, δv_N, and δv_U, respectively. $\delta \boldsymbol{p}_{\text{SINS}}$ is the position error of the SINS, which is composed of latitude error δL, longitude error $\delta \lambda$, and height error δh.

$\boldsymbol{\varepsilon}_{ib}^{b}$ and $\boldsymbol{\nabla}_{ib}^{b}$ represent the constant biases of the gyroscopes and accelerometers, respectively.

The SINS error equation is expressed as follows:

$$\dot{\boldsymbol{\phi}}_n = \boldsymbol{\phi}_n \times \boldsymbol{\omega}_{in}^n + \delta\boldsymbol{\omega}_{in}^n - \boldsymbol{C}_b^n \boldsymbol{\varepsilon}_{ib}^b \tag{2}$$

$$\delta\dot{\boldsymbol{v}}_{\text{SINS}}^n = -\boldsymbol{\phi}_n \times \boldsymbol{f}^n + \delta\boldsymbol{v}_{\text{SINS}}^n \times \left(2\boldsymbol{\omega}_{ie}^n + \boldsymbol{\omega}_{en}^n\right)$$
$$+ \boldsymbol{v}_{\text{SINS}}^n \times \left(2\delta\boldsymbol{\omega}_{ie}^n + \delta\boldsymbol{\omega}_{en}^n\right) + \boldsymbol{C}_b^n \boldsymbol{\nabla}_{ib}^b + \delta\boldsymbol{g}^n \tag{3}$$

$$\delta\dot{L} = \delta v_N/(R_M + h) - v_N\delta h/(R_M + h)^2 \tag{4}$$

$$\delta\dot{\lambda} = \sec L\delta v_E/(R_N + h) + v_E\tan L\sec L\delta L/(R_N + h)$$
$$- v_E\sec Lh/(R_N + h)^2 \tag{5}$$

$$\delta\dot{h} = \delta v_U \tag{6}$$

$$\dot{\boldsymbol{\varepsilon}}_{ib}^b = \mathbf{0}_{3\times 1} \tag{7}$$

$$\dot{\boldsymbol{\nabla}}_{ib}^b = \mathbf{0}_{3\times 1} \tag{8}$$

where $\boldsymbol{C}_b^n$ represents the transformation matrix from the b frame to the n frame. $\boldsymbol{\omega}_{in}^n$ represents the angular rate of the n frame relative to the inertial frame as observed in the n frame. $\boldsymbol{\omega}_{en}^n$ denotes the angular rate from the n frame to the earth frame within the n frame, while $\boldsymbol{\omega}_{ie}^n$ denotes the earth rotation rate in the n frame. $\delta\boldsymbol{g}^n$ refers to the gravity disturbance error. $\boldsymbol{f}^n$ indicates the specific force in the n frame. R_M and R_N are the principal radius of curvature for the prime meridian and equator, respectively. $(\cdot)\times$ is employed to resolve the antisymmetric matrix, δ represents the corresponding error of the parameters, and $\mathbf{0}_{i\times j}$ denotes the $i \times j$ zero matrix.

The error state equation of the SINS/2D-LDV tightly coupled system can be formulated as

$$\dot{\boldsymbol{x}}_k = \boldsymbol{F}_k\boldsymbol{x}_k + \boldsymbol{G}_k\boldsymbol{w}_k \tag{9}$$

where $\boldsymbol{F}_k$, $\boldsymbol{G}_k$, and $\boldsymbol{w}_k$ represent the system state transition matrix, the noise transfer matrix, and the system noise vector, respectively. The specific forms of these matrices and vectors are detailed in [38].

B. Measurement Equation Model

In SINS/2D-LDV tightly coupled integration, the navigation filter uses the velocity difference between the LDV and the SINS as velocity observation. Therefore, it is necessary to unify the coordinate systems by projecting the SINS output velocity in the n frame onto the frame of the 2D-LDV beam velocity. The frame of the 2D-LDV beam velocity is defined as the beam frame, which consists of the two measurement beams of the 2D-LDV and a virtual beam perpendicular to the plane formed by the two measurement beams. The direction of the virtual beam aligns with the x_m axis direction in the m frame shown in Fig. 2, and its measurement value is always zero to satisfy the vehicle's lateral zero-velocity constraint. The beam relationship of the 2D-LDV and the relationship between the beam frame and the m frame are illustrated in Fig. 3.

In Fig. 3, θ_1 and θ_2 represent the inclination angles of the two beams of 2D-LDV, while θ denotes the included angle between the bisector of the two measurement beams and each individual beam. v_{beam1}, v_{beam2}, and v_{beam3} are the measured velocities of the first and second measurement beams (Beam1 and Beam2) and the virtual beam of the 2D-LDV, respectively. v_x^m, v_y^m, and v_z^m represent the velocities in three orthogonal
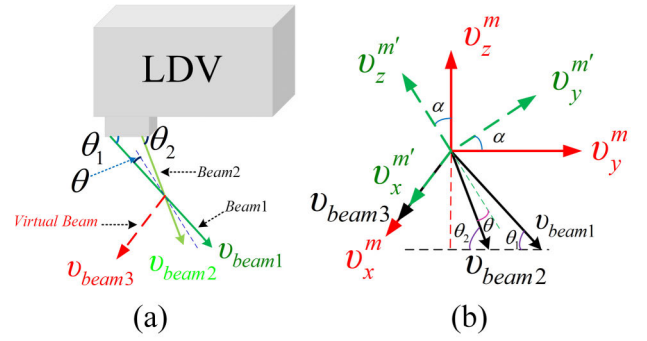

Fig. 3. (a) Beam relationship of 2D-LDV. (b) Relationship between the beam frame and m frame.

directions of the m frame. Similarly, $v_x^{m'}$, $v_y^{m'}$, and $v_z^{m'}$ denote the velocities in three orthogonal directions of the m' frame, where the m' frame is an intermediate frame between the beam frame and the m frame, defined as follows: The angle bisector of the two outgoing beams is designated as the z-axis, with the upward direction being positive. The perpendicular line to the z-axis within the plane formed by the two outgoing beams is defined as the y-axis, with the forward direction being positive. Lastly, the x-axis is determined by the right-hand rule.

According to the definitions of the m' frame and the m frame, a rotational relationship exists between the two. Specifically, the m' frame rotates clockwise around the x-axis by an angle α to align with the m frame. The angle α is determined as follows:

$$\alpha = \frac{\pi - (\theta_1 + \theta_2)}{2}. \tag{10}$$

Remark 1: Once the inclination angles of the two beams of 2D-LDV are determined, the installation relationship between the beam frame and the m frame is also established. However, as shown in Fig. 3, the connection between these two frames is not immediately intuitive. Introducing and defining the m' frame clarifies the relationship between the beam frame and the m frame, making it easier to understand.

From Fig. 3(b), the following transformation relationship exists between the velocities in the beam frame and the m frame:

$$\boldsymbol{v}^{\text{beam}} = \left[v_{\text{beam1}} \; v_{\text{beam2}} \; v_{\text{beam3}} \right]^T = \boldsymbol{C}_{m'}^{\text{beam}}\boldsymbol{v}^{m'} = \boldsymbol{C}_{m'}^{\text{beam}}\boldsymbol{C}_{\alpha x}^T\boldsymbol{v}^m \tag{11}$$

where $\boldsymbol{v}^{\text{beam}}$, $\boldsymbol{v}^{m'}$, and $\boldsymbol{v}^m$ represent the true velocity in the beam frame, m' frame, and m frame, respectively. $\boldsymbol{C}_{m'}^{\text{beam}}$ and $\boldsymbol{C}_{\alpha x}$ denote the transformation matrix from the m' frame to the beam frame and the elemental rotation matrix about the x-axis, respectively, and are denoted as follows:

$$\boldsymbol{C}_{m'}^{\text{beam}} = \begin{bmatrix} 0 & \sin\theta & -\cos\theta \\ 0 & -\sin\theta & -\cos\theta \\ 1 & 0 & 0 \end{bmatrix} \tag{12}$$

$$\boldsymbol{C}_{\alpha x} = \begin{bmatrix} 1 & 0 & 0 \\ 0 & \cos\alpha & -\sin\alpha \\ 0 & \sin\alpha & \cos\alpha \end{bmatrix}. \tag{13}$$

Based on the preceding analysis, the velocity of SINS in the beam frame is

$$\tilde{\boldsymbol{v}}_{\text{SINS}}^{\text{beam}} = \boldsymbol{C}_{m'}^{\text{beam}} \boldsymbol{C}_{\alpha x}^{T} \boldsymbol{C}_{b}^{m} \tilde{\boldsymbol{C}}_{n}^{b} \tilde{\boldsymbol{v}}_{\text{SINS}}^{n} \tag{14}$$

where $\tilde{\boldsymbol{v}}_{\text{SINS}}^{n}$ is the SINS output velocity in the n frame. $\boldsymbol{C}_{b}^{m}$ denotes the attitude transformation matrix from the b frame to the m frame. $\tilde{\boldsymbol{C}}_{n}^{b}$ represents the error-contaminated attitude transformation matrix from the n frame to the b frame. The specific form of the above two attitude transformation matrices is as follows:

$$\tilde{\boldsymbol{C}}_{n}^{b} \approx \boldsymbol{C}_{n}^{b}(\boldsymbol{I}_{3} + \boldsymbol{\phi}_{n} \times) \tag{15}$$

$$\boldsymbol{C}_{b}^{m} \approx (\boldsymbol{I}_{3} + \boldsymbol{\phi}_{m} \times) \tag{16}$$

where $\boldsymbol{I}_{3}$ represents the identity matrix of size three. $\boldsymbol{\phi}_{m}$ denotes the installation misalignment angle between the m frame and the b frame. Generally, the installation misalignment angle can be obtained by calibration before using the SINS/2D-LDV integration.

The 2D-LDV output velocity in the beam frame is defined as

$$\tilde{\boldsymbol{v}}_{\text{LDV/NHC}}^{\text{beam}} = \begin{bmatrix} \tilde{v}_{\text{beam1}} & \tilde{v}_{\text{beam2}} & 0 \end{bmatrix}^{T} = \boldsymbol{v}^{\text{beam}} + \boldsymbol{v}_{D} \tag{17}$$

where $\boldsymbol{v}_{D}$ is the measurement noise vector defined as

$$\boldsymbol{v}_{D} = \begin{bmatrix} v_{\text{beam1}} & v_{\text{beam2}} & v_{\text{NHC}} \end{bmatrix}^{T} \tag{18}$$

where v_{beam1} and v_{beam1} represent the measurement noise of the two 2D-LDV beams and v_{NHC} denotes the noise associated with the NHC lateral zero-velocity constraint.

The measurement equation of the SINS/2D-LDV tightly coupled system is established as follows:

$$\boldsymbol{z}_{k} = \tilde{\boldsymbol{v}}_{\text{LDV/NHC}}^{\text{beam}} - \tilde{\boldsymbol{v}}_{\text{SINS}}^{\text{beam}} = \boldsymbol{H}_{k} \boldsymbol{x}_{k} + \boldsymbol{v}_{k} \tag{19}$$

where $\boldsymbol{v}_{k} = \boldsymbol{v}_{D}$ denotes the measurement noise, while $\boldsymbol{z}_{k}$ and $\boldsymbol{H}_{k}$ represent the measurement vector and the measurement transition matrix, respectively, and can be expressed as follows:

$$\begin{aligned} \boldsymbol{z}_{k} &= \tilde{\boldsymbol{v}}_{\text{LDV/NHC}}^{\text{beam}} - \tilde{\boldsymbol{v}}_{\text{SINS}}^{\text{beam}} \\ &= \boldsymbol{v}^{\text{beam}} + \boldsymbol{v}_{D} - \boldsymbol{C}_{m'}^{\text{beam}} \boldsymbol{C}_{\alpha x}^{T} \boldsymbol{C}_{b}^{m} \tilde{\boldsymbol{C}}_{n}^{b} \tilde{\boldsymbol{v}}_{\text{SINS}}^{n} \\ &\approx \boldsymbol{v}^{\text{beam}} - \boldsymbol{C}_{m'}^{\text{beam}} \boldsymbol{C}_{\alpha x}^{T} \boldsymbol{C}_{b}^{m} \boldsymbol{C}_{n}^{b}(\boldsymbol{I}_{3} + \boldsymbol{\phi}_{n} \times)(\boldsymbol{v}^{n} + \delta\boldsymbol{v}_{\text{SINS}}^{n}) + \boldsymbol{v}_{D} \\ &\approx \boldsymbol{C}_{m'}^{\text{beam}} \boldsymbol{C}_{\alpha x}^{T} \boldsymbol{C}_{b}^{m} \boldsymbol{C}_{n}^{b}(\boldsymbol{v}^{n} \times) \boldsymbol{\phi}_{n} - \boldsymbol{C}_{m'}^{\text{beam}} \boldsymbol{C}_{\alpha x}^{T} \boldsymbol{C}_{b}^{m} \boldsymbol{C}_{n}^{b} \delta\boldsymbol{v}_{\text{SINS}}^{n} + \boldsymbol{v}_{D} \end{aligned} \tag{20}$$

$$\boldsymbol{H}_{k} = \begin{bmatrix} \boldsymbol{C}_{m'}^{\text{beam}} \boldsymbol{C}_{\alpha x}^{T} \boldsymbol{C}_{b}^{m} \boldsymbol{C}_{n}^{b}(\boldsymbol{v}^{n} \times) & -\boldsymbol{C}_{m'}^{\text{beam}} \boldsymbol{C}_{\alpha x}^{T} \boldsymbol{C}_{b}^{m} \boldsymbol{C}_{n}^{b} & \boldsymbol{0}_{3 \times 9} \end{bmatrix} \tag{21}$$

where $\boldsymbol{v}^{n}$ denotes the true velocity in the n frame.

III. MEASUREMENT VALUE PREDICTION SCHEME BASED ON THE LSTM NETWORK

In current SINS/LDV integrated navigation methods, the measurement noise covariance matrix is usually enlarged to mitigate the effects of NHC violations and LDV outliers on the system [20]. However, this method is insufficient for prolonged LDV failures, and the intricate nonlinear relationships between NHC, LDV measurements, and various factors (including vehicle dynamics, as well as the installation
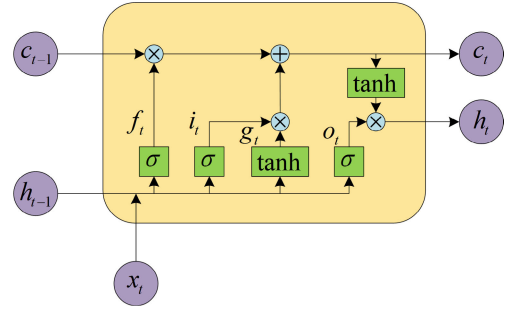

Fig. 4. Structure of the basic LSTM cell.

position and angle of the LDV and the IMU) often result in suboptimal adjustments of the measurement noise covariance matrix, which fails to fully exploit the observed values for suppressing SINS errors [24]. Moreover, the expansion of the measurement noise covariance matrix may lead to a loss of constraint information from measurement values. Given DL's superior ability to independently learn the complex, implicit associations between IMU outputs, vehicle motion states, and LDV outputs, it is possible to extract and exploit the inherent coupling relationships through DL methods. Accordingly, this section uses the widely recognized LSTM method in DL to estimate the vehicle lateral velocity and the LDV output.

A. Basic Principles of LSTM

LSTM is a variant of RNN capable of learning and storing long-term input trends, which can work well with time series data. The traditional RNN structure can be seen as a "loop" comprising a series of neurons, with each neuron receiving input data and generating output, which is then passed on as input to the next neuron. This structure facilitates the learning of short-term dependencies within sequential data. However, due to the challenges of vanishing and exploding gradients, RNNs are less effective with long sequences. LSTM networks address this limitation by introducing memory cells, input gates, output gates, and forget gates. The memory cell retains crucial information, the input gate determines whether to store current input data in the memory cell, the forget gate determines the retention or discarding of information within the memory cell, and the output gate determines whether to use the information in the memory cell as the current output. The control of these gates enables LSTM to effectively capture important long-term dependencies in sequences and mitigate gradient-related issues. The basic LSTM cell structure is shown in Fig. 4. f_{t}, i_{t}, and o_{t} represent the forget gate, input gate, and output gate, respectively. c_{t} denotes the state memory cell. x_{t} and h_{t} are the input information and intermediate output, respectively. g_{t} represents the candidate memory cell. σ and tanh denote the activation function. t and $t-1$ represent the current moment and the previous moment. The specific calculation formula of the LSTM is shown by

$$f_{t} = \sigma(W_{fx}x_{t} + W_{fh}h_{t-1} + b_{f}) \tag{22}$$

$$i_{t} = \sigma(W_{ix}x_{t} + W_{ih}h_{t-1} + b_{i}) \tag{23}$$

$$g_{t} = \tanh(W_{gx}x_{t} + W_{gh}h_{t-1} + b_{g}) \tag{24}$$

$$o_{t} = \sigma(W_{ox}x_{t} + W_{oh}h_{t-1} + b_{o}) \tag{25}$$

$$c_t = f_t \odot c_{t-1} + i_t \odot g_t \qquad (26)$$

$$h_t = o_t \odot \tanh(c_t) \qquad (27)$$

where W_{fx}, W_{fh}, and b_f denote the weight and bias of the forget gate, respectively. W_{ix}, W_{ih}, and b_i refer to the weight and bias of the input gate, respectively. W_{ox}, W_{oh}, and b_o represent the weight and bias of the output gate, respectively. W_{gx}, W_{gh}, and b_g denote the weight and bias of the candidate memory cell, respectively. $\odot$ denotes the Hadamard product [39], [40].

B. NHC Lateral Velocity Prediction Based on LSTM

In the construction of an LSTM model, the selection of appropriate parameters for inputs and outputs is crucial for improving training efficiency and enhancing prediction accuracy. Given that our objective is to predict the vehicle's lateral velocity, this parameter serves as the output for both the training and prediction samples. For the training samples, the vehicle's lateral velocity, in the presence of GNSS data, is derived from the projection of the SINS/GNSS integration's velocity onto the vehicle frame (denoted as the m frame in this article). In scenarios where GNSS is unavailable, this velocity is obtained by projecting the first few minutes of velocity output from the pure inertial mode of the SINS onto the vehicle frame.

To ascertain the input features of the LSTM model, it is essential to identify the variables associated with the vehicle's lateral velocity within the integrated navigation system. According to the Coriolis theorem, the equation describing the velocity rate in the b frame is formulated as follows:

$$\dot{\boldsymbol{v}}^b = \boldsymbol{f}^b - \left(\boldsymbol{\omega}_{ie}^b + \boldsymbol{\omega}_{ib}^b\right) \times \boldsymbol{v}^b + \boldsymbol{g}^b \qquad (28)$$

where $\boldsymbol{v}^b$ denotes the velocity in the b frame. $\boldsymbol{f}^b$ and $\boldsymbol{\omega}_{ib}^b$ denote the specific force and body angular rate measured by the accelerometers and gyroscopes in the b frame, respectively. $\boldsymbol{\omega}_{ie}^b$ and $\boldsymbol{g}^b$ represent the projections of the Earth's rotation rate and the gravity vector in the b frame, respectively. Given the negligible magnitude of $\boldsymbol{\omega}_{ie}^b$ relative to $\boldsymbol{\omega}_{ib}^b$ during vehicle motion, it can be ignored, thereby simplifying (28) to

$$\dot{\boldsymbol{v}}^b \approx \boldsymbol{f}^b - \boldsymbol{\omega}_{ib}^b \times \boldsymbol{v}^b + \boldsymbol{g}^b. \qquad (29)$$

The projection of the gravity vector in the b frame is given by

$$\boldsymbol{g}^b = \begin{bmatrix} g \cos\varphi_x \sin\varphi_y \\ -g \sin\varphi_x \\ -g \cos\varphi_x \cos\varphi_y \end{bmatrix} \qquad (30)$$

where g is the gravity acceleration. φ_x and φ_y denote the pitch and roll angles of the system, respectively.

Similar to (29), the equation for velocity rate in the m frame can be expressed as

$$\dot{\boldsymbol{v}}^m \approx \boldsymbol{C}_b^m \boldsymbol{f}^b - \left(\boldsymbol{C}_b^m \boldsymbol{\omega}_{ib}^b\right) \times \boldsymbol{v}^m + \boldsymbol{C}_b^m \boldsymbol{g}^b. \qquad (31)$$

Based on (31), the velocity in the m frame at time k can be written as

$$\boldsymbol{v}_k^m \approx \boldsymbol{v}_{k-1}^m + \boldsymbol{C}_b^m \Delta\boldsymbol{v}_k$$
$$- \int_{k-1}^{k} \left(\boldsymbol{C}_b^m \boldsymbol{\omega}_{ib}^b(t)\right) \times \boldsymbol{v}^m(t)dt + \boldsymbol{C}_b^m \boldsymbol{g}_{k-\frac{1}{2}}^b T \qquad (32)$$

where $\Delta\boldsymbol{v}_k$ represents the velocity increment measured by the accelerometer within the unit time period T, with the subscript k indicating the corresponding moment.

In (32), $\boldsymbol{C}_b^m$ is derived from the installation misalignment angle of the IMU, which remains relatively stable over extended periods. Furthermore, in land vehicles, the pitch and roll angles are less variable and the variation in gravity acceleration is small in most scenarios. Hence, the main variables affecting lateral acceleration in the m frame are $\boldsymbol{f}^b$, $\boldsymbol{\omega}_{ib}^b$, υ_y^m, and υ_z^m.

In conclusion, the relationship between the input features and the vehicle's lateral velocity in the m frame can be expressed as follows:

$$\upsilon_x^m = \upsilon_{\text{beam3}} = \text{LSTM}^1\left(\boldsymbol{f}^b, \boldsymbol{\omega}_{ib}^b, \upsilon_y^m, \upsilon_z^m\right). \qquad (33)$$

C. 2D-LDV Beam Velocity Prediction Based on LSTM

Equation (14) gives the relationship between the velocity in the beam frame and the velocity in the n frame. It is evident that the velocity in the beam frame predominantly correlates with the system output's attitude and velocity. Following the velocity update equation of SINS, the velocity in the n frame at time k can be written as:

$$\boldsymbol{v}_k^n = \boldsymbol{v}_{k-1}^n + \Delta\boldsymbol{v}_{f,k}^n + \Delta\boldsymbol{v}_{g/\text{cor},k}^n \qquad (34)$$

where $\Delta\boldsymbol{v}_{f,k}^n$ and $\Delta\boldsymbol{v}_{g/\text{cor},k}^n$ denote the specific force integral and the gravity/Coriolis velocity integral, respectively, and are expressed as follows:

$$\Delta\boldsymbol{v}_{f,k}^n = \boldsymbol{C}_{b(k-1)}^n \Delta\boldsymbol{v}_k - \frac{T}{2}\boldsymbol{\omega}_{in,k-\frac{1}{2}}^n \times \left(\boldsymbol{C}_{b(k-1)}^n \Delta\boldsymbol{v}_k\right)$$
$$+ \boldsymbol{C}_{b(k-1)}^n \left(\frac{1}{2}\Delta\boldsymbol{\theta}_k \times \Delta\boldsymbol{v}_k + \frac{1}{2}\int_{k-1}^{k} \left\{\Delta\boldsymbol{\theta}(t)\right.\right.$$
$$\left.\left. \times \boldsymbol{f}^b(t) + \Delta\boldsymbol{v}(t) \times \boldsymbol{\omega}_{ib}^b(t)\right\}dt\right) \qquad (35)$$

$$\Delta\boldsymbol{v}_{g/\text{cor},k}^n = \left\{-\left[2\boldsymbol{\omega}_{ie}^n + \boldsymbol{\omega}_{en}^n\right] \times \boldsymbol{v}^n + \boldsymbol{g}^n\right\}_{k-\frac{1}{2}} T \qquad (36)$$

where $\Delta\boldsymbol{\theta}_k$ represents the angular increment measured by the gyroscope within the unit time period T.

According to (14) and (34)–(36), it is readily apparent that the main variables influencing the velocity in the beam frame include the system's attitude, angular velocity, velocity, and specific force. Therefore, the relationship between the input features and the beam velocity of the 2D-LDV can be expressed as

$$(\upsilon_{\text{beam1}}, \upsilon_{\text{beam2}}) = \text{LSTM}^2\left(f^b, \omega_{ib}^b, \upsilon^n, \boldsymbol{\varphi}\right) \qquad (37)$$

where $\boldsymbol{\varphi}$ is the Euler angle corresponding to $\boldsymbol{C}_b^n$.

IV. FAULT DETECTION METHOD AND ADAPTIVE FILTER

While the DL method can predict both the vehicle's lateral velocity and the 2D-LDV's beam measurement value, ensuring accurate use of these predicted values is critical to improving the robustness and accuracy of the integrated navigation system in practical scenarios. Thus, it is imperative to employ a reliable method to accurately discriminate the vehicle sideslip and the validity of the 2D-LDV output to ensure timely use of predicted values to mitigate system

errors when the vehicle's NHC is violated and the LDV output is abnormal. The chi-square detection-based outlier discrimination method is widely used in integrated navigation, and its detection performance is closely related to the test statistic and threshold. However, when the error distribution is non-Gaussian or the outliers are inconspicuous, the chi-square method may result in a missed or false detection. The LOF is a density-based outlier detection technique that detects outliers without any specific distributional assumptions, and it has seen extensive application in power system testing and machinery health monitoring [41], [42]. Therefore, this section introduces the LOF into the SINS/2D-LDV integration to monitor the outputs of the vehicle NHC and the 2D-LDV. Upon detecting outliers, substituting the LSTM network predicted values for outliers, and the measurement noise covariance matrix is adaptively adjusted according to the innovation residuals, further improving the robustness of the system.

A. Local Outlier Factor

The LOF quantifies the degree of outliers by assessing the density between an object and its neighborhood objects, recognized as a prominent unsupervised data mining technique. The specific calculation procedure of the LOF is as follows steps [43].

Step 1 (Define the K-Distance): For an object p in dataset D, given a positive integer K, its K-distance, denoted as $K\text{dis}(p)$, is defined as the distance $\text{dis}(p, q)$ between p and another object q within dataset D, such that:

1) for at least K objects $q' \in D/\{p\}$, satisfy $\text{dis}(p, q') \le \text{dis}(p, q)$.
2) for at most $K - 1$ objects $q' \in D/\{p\}$, satisfy $\text{dis}(p, q') < \text{dis}(p, q)$.

Step 2 (Define the K-Distance Neighborhood): For an object p in dataset D, its K-distance neighborhood is defined as a set in D that includes objects (e.g., q) whose distance from p is not greater than the K-distance of p, that is,

$$N_k(p) = \{q \in D/\{p\}|\text{dis}(p, q) \le K\text{dis}(p)\}. \tag{38}$$

Step 3 (Define the Reachable Distance): Given two objects p and q in dataset D, the reachable distance of object p with respect to object q is defined as the maximum of the K-distance of q and the distance between the p and q, as defined by the following formula:

$$\text{reach} - \text{dis}_k(p, q) = \max\{K\text{dis}(q), \text{dis}(p, q)\}. \tag{39}$$

Step 4: In conjunction with the above steps, the local reachable density of p can be calculated by the following equation:

$$lrd_k(p) = \left(\frac{1}{k} \sum_{q \in N_k(p)} \text{reach} - \text{dis}_k(p, q)\right)^{-1}. \tag{40}$$

According to (39) and (40), if object p significantly deviates from its neighboring objects, its neighborhood will encompass fewer objects and will not be included in the neighborhood of other objects, which results in the local reachability density of p is smaller compared to that of other normal objects.

Consequently, the local reachability density represents the degree of object aggregation within a specified neighborhood.

Step 5: Based on the definition of the local reachable density, the LOF value of the object p is calculated to assess its degree of abnormality. It is given by

$$\text{LOF}_k(p) = \frac{1}{k} \sum_{q \in N_k(p)} \frac{lrd_k(q)}{lrd_k(p)}. \tag{41}$$

From the LOF calculation steps described above, it is evident that the LOF of p is the average of the ratios between the local reachability density of p and that of its K-nearest neighbors. If p is a normal value, it shares similar properties with its K-nearest neighbors, resulting in an LOF value close to 1. Conversely, if p is an outlier, its local reachability density will be lower than that of its K-nearest neighbors, leading to an LOF value significantly greater than 1.

B. Fault Detection Solution

When a vehicle experiences sideslip or the beam measurements from the 2D-LDV are abnormal, the corresponding measurement vector z_k will contain the abnormal data, and then the filter innovation vector will be affected by the outliers. Therefore, the innovation vector is selected as the object in the LOF in this article. The filter innovation vector is expressed as follows:

$$e_k = z_k - H_k x_{k|k-1} \tag{42}$$

where $x_{k|k-1}$ represents the one-step prediction of the system state in the Kalman filter.

To precisely identify the location of the outliers, each of the three components of the e_k is detected individually. For simplicity, this article demonstrates the calculation process of LOF using only the first component as an example. The dataset is constructed as follows:

$$D_1 = \begin{bmatrix} e_{k-N+1}(1) & e_{k-N+2}(1) & \cdots & e_k(1) \end{bmatrix} \tag{43}$$

where N denotes the set sample size, that is, the window size of the dataset.

It should be noted that the LDV's output frequency of 100 Hz presents a challenge for the LOF use in the SINS/2D-LDV integration. Specifically, a larger window size enhances the detection accuracy for outliers but also substantially increases the computational load. Conversely, a smaller window size reduces computation but may lead to false detections in the presence of continuous outliers. To address this issue, we construct a dataset $D_h = \{D_{h1}, D_{h2}, D_{h3}\}$ using historical normal data and compare new samples against this dataset during integrated navigation to determine the abnormality of the samples. This allows for effective outlier detection while using a smaller window size.

To enhance the detection accuracy of outliers, data classification was performed during the dataset construction. For the datasets D_{h1} and D_{h2}, consisting of the e_k components related to the velocity of the two beams of the 2D-LDV, and the dataset D_{h3}, consisting of the e_k component related to the

lateral velocity of the vehicle, they were categorized based on the forward velocity of the vehicle, as follows:

$$D_{hj(j=1,2)} = \big\{ D_{hj}(\upsilon_{\text{for}} = 0), D_{hj}(0 < \upsilon_{\text{for}} \leq 5),$$
$$D_{hj}(5 < \upsilon_{\text{for}} \leq 10), D_{hj}(10 < \upsilon_{\text{for}} \leq 15),$$
$$D_{hj}(15 < \upsilon_{\text{for}} \leq 20), D_{hj}(20 < \upsilon_{\text{for}} \leq 25),$$
$$D_{hj}(25 < \upsilon_{\text{for}} \leq 30), D_{hj}(\upsilon_{\text{for}} \geq 30) \big\} \quad (44)$$
$$D_{h3} = \{ D_{h3}(\upsilon_{\text{for}} = 0), D_{h3}(\upsilon_{\text{for}} \neq 0) \} \quad (45)$$

where υ_{for} is the vehicle's forward velocity obtained by the integrated navigation system.

Based on (44) and (45) and the current υ_{for}, (43) can be rewritten as

$$D_1 = \big[\, D_{h1}(\upsilon_{\text{for}}) \quad e_k(1) \, \big]. \quad (46)$$

According to (46), the spatial distance matrix (SDM) corresponding to the dataset D is expressed as follows:

$$SDM = \begin{bmatrix} \text{dis}(D(1), D(1)) & \cdots & \text{dis}(D(1), D(N)) \\ \vdots & \vdots & \vdots \\ \text{dis}(D(M), D(1)) & \cdots & \text{dis}(D(M), D(N)) \\ \vdots & \vdots & \vdots \\ \text{dis}(D(N), D(1)) & \cdots & \text{dis}(D(N), D(N)) \end{bmatrix}$$
$$(47)$$

where M is an integer between 1 and N.

In (47), each row of the SDM contains the Euclidean distances between a given object and all other objects in the dataset. By sorting each row of the SDM in ascending order, the neighborhood set and K-distance of the object can be determined based on the preset number of neighbors.

Finally, the LOF of each object can be obtained according to (39)–(41), denoted as $\text{LOF}_1(e_k(1))$. Similarly, the LOF of the other two components of the innovation vector can be obtained, denoted as $\text{LOF}_2(e_k(2))$ and $\text{LOF}_3(e_k(3))$.

By comparing $\text{LOF}_1(e_k(1))$ and $\text{LOF}_2(e_k(2))$ with their respective thresholds, it can be determined whether there is an anomaly in the two beam measurements of the 2D-LDV. Similarly, by comparing $\text{LOF}_3(e_k(3))$ with its threshold, it can be determined whether the vehicle's NHC has been violated. If the LOF value is less than the threshold, it means that the local density of the current data is close to the historical data, indicating normalcy and allowing filter estimation to continue. Conversely, a higher LOF value suggests errors in the corresponding measurements, prompting the replacement of the original measurements with those predicted by the LSTM network. The new measurement vector is denoted by $\bar{z}_k$.

C. Adaptive Filter

After detecting and replacing the outliers, perform (42) again to update the e_k with $\bar{z}_k$. Considering the potential for significant errors in the measurements predicted by the LSTM model, a series of fading factors are employed to inflate the measurement noise covariance matrix. This adjustment aims to mitigate the impact of LSTM-predicted value errors on the system's filtering precision.

Due to discrepancies between the overall accuracy of the LSTM predicted measurement value and the normal measurement value, the a priori measurement noise covariance matrix is categorized according to whether the LSTM predicted measurement value is used or not

$$R_k = \begin{cases} \text{diag}(\sigma_{\text{normal}}^2), & \text{Not using predicted values} \\ \text{diag}(\sigma_{\text{predict}}^2), & \text{Using predicted values} \end{cases} \quad (48)$$

where σ_{normal}^2 and $\sigma_{\text{predict}}^2$ are the initial variances without and with the predicted velocity, respectively, which can be pregiven according to the measurement accuracy of the LDV and the prediction accuracy of the LSTM model.

The new measurement noise covariance matrix $\hat{R}_k$ has the following relationship with the R_k:

$$\hat{R}_k = S_k R_k S_k^T \quad (49)$$

where $S_k = \text{diag}\{ s_1 \ s_2 \ s_3 \}$, s_l denotes the fading factor associated with the lth measurement component $\bar{z}_k(l)$.

Under the Gaussian assumption, the theoretical covariance of e_k can be written as

$$C_k = H_k P_{k|k-1} H_k^T + R_k \quad (50)$$

where $P_{k|k-1}$ represents the covariance matrix corresponding to $x_{k|k-1}$.

To mitigate disturbances in the system state caused by excessive prediction value errors, the Sage window smoothing method is employed to calculate the covariance matrix of the filter innovation vector. For a given window size L, the prediction covariance matrix of e_k can be calculated as

$$\hat{C}_k = \frac{1}{L} \sum_{d=k-L+1}^{k} e_d e_d^T. \quad (51)$$

According to (50) and (51), the following relation can be obtained:

$$\hat{C}_k = H_k P_{k|k-1} H_k^T + S_k R_k S_k^T. \quad (52)$$

From the above equation, it can be deduced that

$$S_k(l) = \max\left(1, \sqrt{\frac{M_k(l, l)}{R_k(l, l)}} \right), \quad l = 1, 2, 3 \quad (53)$$

where

$$M_k = \hat{C}_k - H_k P_{k|k-1} H_k^T. \quad (54)$$

Based on the results of (53), the measurement noise covariance matrix can be adjusted by (49) to mitigate the impact of LSTM prediction error on the integrated navigation system.

V. EXPERIMENT RESULTS AND ANALYSIS

In Section V, a comprehensive dataset was first collected from the vehicle-mounted SINS/2D-LDV integration to complete the training of the LSTM model and acquire the historical normal data necessary for LOF detection. The performance of the proposed method was then evaluated using two sets of experimental data from long-distance, high-maneuver trials. All data used in this article were obtained from the identical

TABLE I
SPECIFICATIONS OF THE EXPERIMENTAL APPARATUS

Sensor	Performance	Specification
IMU	Gyro bias stability	0.003°/h
	Gyro random walk	0.0005∘/√h
	Accelerometer bias stability	20μg
	Accelerometer random walk	5μg/√h
	Data update rate	100Hz
2D-LDV	Measurement accuracy	0.08%
	Data update rate	100Hz
GNSS	Measurement accuracy	0.1m (RTK)
	Data update rate	10Hz
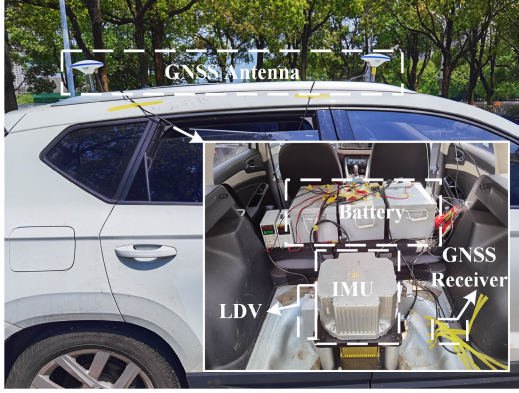
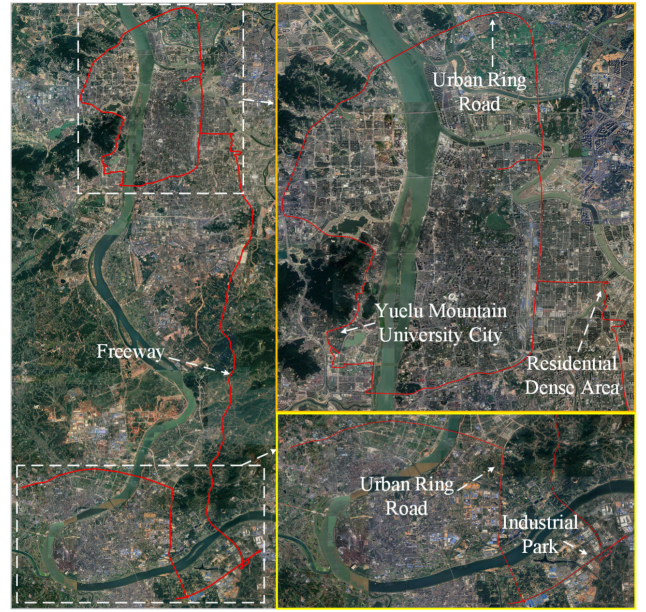Fig. 5. Test vehicle and the experimental system.
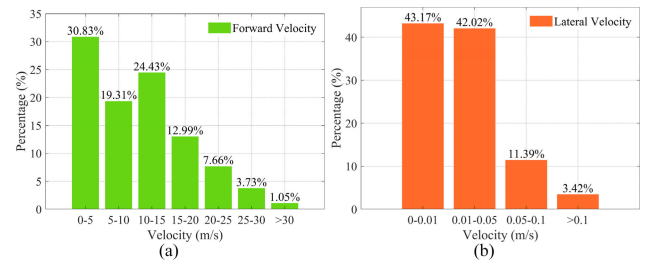

Fig. 6. Vehicle trajectory of the training dataset.

Fig. 7. Distributions of the velocity on the training dataset. (a) Vehicle forward velocity calculated from the two beam velocities of the 2D-LDV. (b) Vehicle lateral velocity obtained from SINS/GNSS integration.

SINS/2D-LDV integration. Fig. 5 illustrates the experimental apparatus, comprising a dual-antenna differential GNSS, a self-developed high-precision IMU, and two homemade 2D-LDVs. The 2D-LDV used in this article is mounted on the left side of the IMU, with its measurement beam tilted forward. The principal parameters of these components are detailed in Table I.

A. Model Training and Dataset Acquisition

The vehicle traveling trajectory in the training dataset is illustrated in Fig. 6. This trajectory spans three regions in Hunan Province: Changsha, Zhuzhou, and Xiangtan. It includes different scenarios, such as freeways, densely populated residential areas, university campuses, industrial parks, and urban ring roads. The labels used for training by the two models were generated from the vehicle lateral velocity obtained by postprocessing the SINS/GNSS integration and the two beam velocities from the 2D-LDV. The distributions of the velocity on label data are shown in Fig. 7, which shows that most of the samples in the dataset have vehicle forward velocities and lateral velocities less than 15 and 0.05 m/s, respectively. Specifically, high-velocity scenarios are represented by freeways and certain urban ring roads, while university campuses and densely populated residential areas constitute low-velocity scenarios. The remaining road sections are categorized as medium-velocity scenarios, with vehicle turns and rapid directional changes denoting sideslip scenarios. The training was conducted on an NVIDIA GeForce RTX 3080 GPU. The LSTM network architecture encompasses an input layer, an LSTM layer with 200 hidden units,

a dropout layer with a dropout probability of 0.2, a fully connected layer, and an output layer. Utilizing the Adam optimizer [44], the network underwent training for 1000 epochs. The initial learning rate was set to 0.005, with a decay factor of 0.5. The training batch size was 128, and the mean square error obtained from the difference between the predicted and actual values was used as the loss function.

In accordance with the velocity classification depicted in Fig. 7(a), the historical innovation vector data required for LOF detection can be obtained by the SINS/2D-LDV integration. To ensure the normality of the historical data, the LDV output and the vehicle motion state were initially assessed to filter out abnormal data. Thus, the historical innovation vector data necessary for LOF detection was acquired under conditions of normal LDV output and the absence of vehicle sideslip. As explained in Section IV-B, constructing a historical dataset using the system's normal data and classifying it based on different vehicle velocities enables effective outlier detection, even with a smaller data window. Given the system's 100-Hz data update rate, the LOF detection window size was set to 100 to improve detection efficiency (a larger window size may be selected if the navigation computer's performance permits). During each detection process, 99 values are randomly selected from the historical dataset based on the
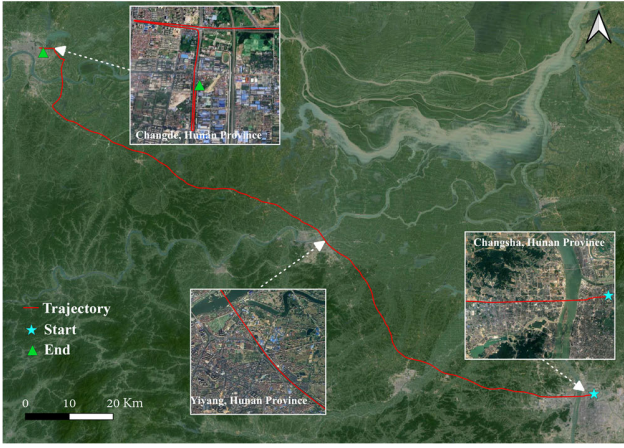
Fig. 8. Vehicle trajectory in the first experiment.

TABLE II
COMPARISON OF THE PERFORMANCE OF THE FIVE METHODS IN THE FIRST EXPERIMENT (177.27 km)

Methods		RMSE (m, ‰)		Max (m, ‰)	
Method 1	Horizontal error	9.61	0.054	18.04	0.102
	Height error	7.36	0.042	13.13	0.074
Method 2	Horizontal error	8.53	0.048	15.17	0.086
	Height error	0.75	0.004	2.42	0.013
Method 3	Horizontal error	7.79	0.044	13.25	0.075
	Height error	0.71	0.004	2.14	0.012
Method 4	Horizontal error	6.14	0.035	12.11	0.068
	Height error	0.62	0.003	1.61	0.009
Method 5	Horizontal error	**5.78**	**0.033**	**11.78**	**0.066**
	Height error	**0.57**	**0.003**	**1.26**	**0.007**

For RMSE and Max, the left column represents absolute errors, while the right column represents relative errors.

vehicle's current velocity to determine if the current data is normal. As described in Section IV-A, the LOF calculates the density deviation between a data point and its neighbors. If the density of a data point is significantly lower than that of its neighbors, it is considered an outlier. Thus, the choice of the LOF's neighborhood value and detection threshold directly affects outlier detection accuracy. In this article, the LOF neighborhood value K was set to 75, with the detection thresholds for $\text{LOF}_1(e_k(1))$ and $\text{LOF}_2(e_k(2))$ set to 7.5 and for $\text{LOF}_3(e_k(3))$ set to 3. These values are determined based on the principles of LOF and engineering experience. Since the vehicle's lateral velocity is much smaller than the two measurement values of the 2D-LDV, the threshold for $\text{LOF}_3(e_k(3))$ was set lower than those for $\text{LOF}_1(e_k(1))$ and $\text{LOF}_2(e_k(2))$. Some details on the selection of LOF parameters can be found in [43].

B. Performance Evaluation

To evaluate the performance of the proposed SINS/2D-LDV tightly coupled integration scheme, five methods were designed for comparison.

Method 1: The traditional SINS/LDV integration approach, where LDV provides only the forward velocity of the vehicle.

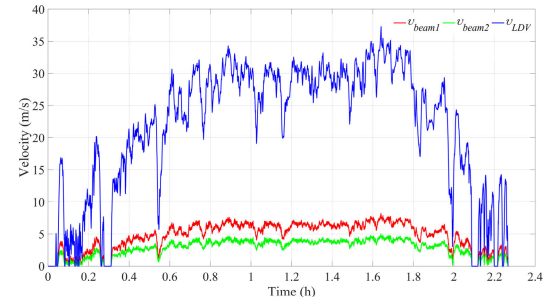*Method 2:* The SINS/2D-LDV tightly coupled approach is explicated in Section II.

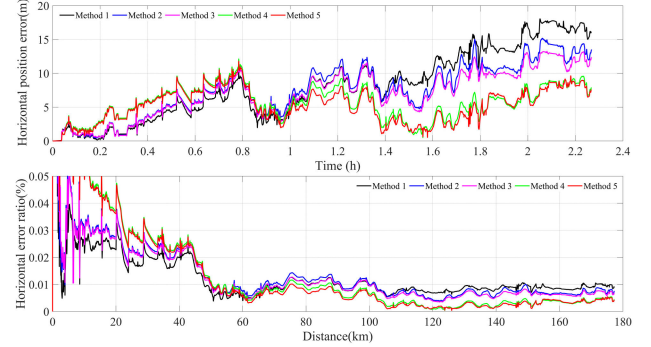Fig. 9. LDV velocity output curve in the first experiment.

Fig. 10. Horizontal location error of the first experiment. The top is the absolute position estimation error and the bottom is the relative position error.
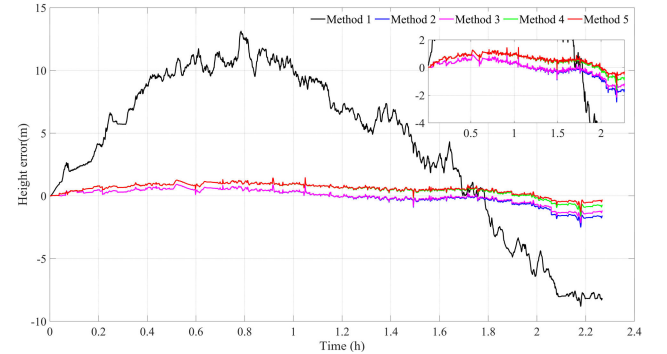

Fig. 11. First experiment's height positioning error.

Method 3: This method, an extension of Method 2, involves identifying outliers in the lateral velocity of the vehicle using LOF and subsequently replacing them with predictions from LSTM.

Method 4: Building upon Method 2, this approach detects outliers in both 2D-LDV beam measurements and replaces them with LSTM-predicted measurements.

Method 5: The integrated navigation method proposed in this article.

The first set of experiments lasted approximately 2.28 h with a total distance of 177.25 km. The trajectory of the vehicle and the output velocity of the 2D-LDV are illustrated in Figs. 8 and 9, respectively, with v_{LDV} in Fig. 9 representing the 1-D velocity calculated from the two beam velocities of the 2D-LDV. Figs. 10 and 11 depict the horizontal and vertical positioning accuracies of different methods, respectively. Table II presents the corresponding maximum (Max)
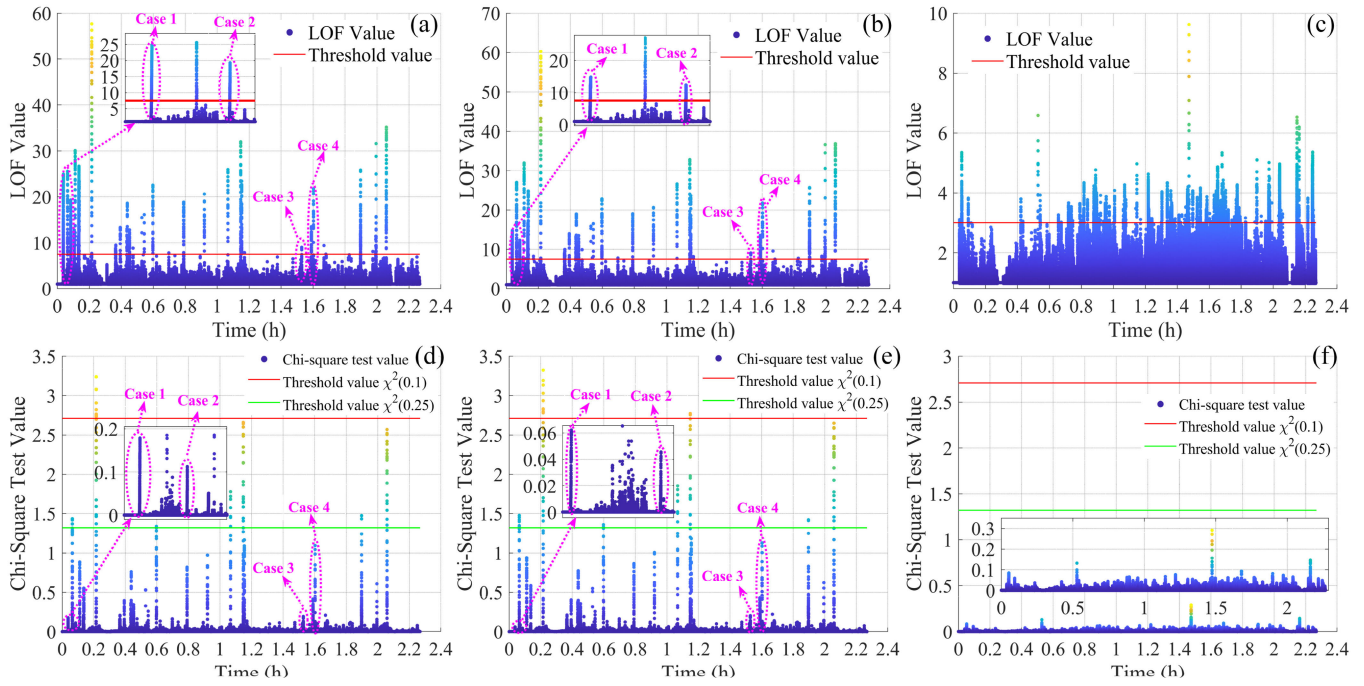
Fig. 12. Abnormal data detection results. (a) $LOF_1(e_k(1))$. (b) $LOF_2(e_k(2))$. (c) $LOF_3(e_k(3))$. (d) Chi-square test value based on $e_k(1)$. (e) Chi-square test value based on $e_k(2)$. (f) Chi-square test value based on $e_k(3)$.

and root mean square error (RMSE) of position errors. The five methods demonstrate satisfactory accuracy, with both the maximum horizontal positioning error being almost less than 0.1‰ of the total distance. These positioning results reflect the exceptional performance of LDV, where its ultrahigh measurement precision and scale factor stability enhance the capability of the SINS/LDV integration for high-precision positioning overextended distances. Method 2 has slightly better horizontal accuracy than Method 1 and significantly better vertical positioning accuracy. This improvement is because the vehicle's vertical velocity in Method 2 is measured by 2D-LDV, which is substantially more accurate than the vertical zero-velocity constraint employed in Method 1. Methods 3, 4, and 5 demonstrate superior positioning accuracy compared to Method 2, with Method 5 exhibiting the highest positioning accuracy. This underscores the efficacy of the proposed LOF-based outlier detection method, which effectively identifies violations of NHC lateral constraints and detects outliers in the 2D-LDV output. Additionally, the LSTM network constructed in this article effectively predicts the lateral velocity of the vehicle and the measurement values of 2D-LDV, contributing to the superior performance of Methods 3, 4, and 5 over Method 2.

To further demonstrate the superiority of the proposed method, particularly its fault detection capability in SINS/2D-LDV tightly coupled integration, Fig. 12 illustrates the outlier detection results of the LOF-based method and the commonly used residual chi-square test based on the Mahalanobis distance for the first set of experiments. Both methods detect the three components of the innovation vector individually. Fig. 13 shows the filter measurement vector used by Methods 5 and 2. The detection results reveal that the proposed method is more sensitive to dataset outliers than the traditional residual

chi-square test. In most integrated navigation systems, the threshold for identifying outliers using the chi-square test is typically set greater than $\chi^2(0.1)$, where 0.1 represents the significance level [45]. When the chi-square test threshold is set to 2.71 ($\chi^2(0.1)$), during the first vehicle test, it detects only a few 2D-LDV measurement outliers and fails to identify the vehicle's lateral zero-velocity violation. This is because, during the experiment, there were no significant anomalies in the 2D-LDV, and the vehicle's side-slip was not severe. The residual chi-square test method is more effective in detecting abrupt faults but is less sensitive to slow-varying faults. Four outlier cases are selected to validate the effectiveness of the proposed method. As shown in Fig. 13, Cases 1 and 2 occur during vehicle start and stop when the vehicle velocity is very low, causing LDV to fail in measuring the velocity value—a common issue in LDV, where the Doppler signal is obscured by noise due to poor signal quality at low velocities. Cases 3 and 4 arise during vehicle movement, representing scenarios where velocity is maintained when the LDV signal is poor—an anomaly common in LDV. Fig. 12 shows that the proposed method accurately detects all four selected cases, whereas the residual chi-square test method fails to detect them accurately, even with a threshold ($\chi^2(0.25)$) set much lower than the empirical value. Additionally, details from the four cases in Fig. 13 reveal that the LSTM network constructed in this article achieves an accurate prediction of LDV output in the presence of LDV outliers. Fig. 13 also shows that the proposed method can detect significant lateral velocity changes in the vehicle and provide relatively accurate predictions, unlike Method 2, which consistently has a lateral velocity of zero due to lateral constraints. This discrepancy explains why the positioning accuracy of Method 3 is better than that of Method 2.
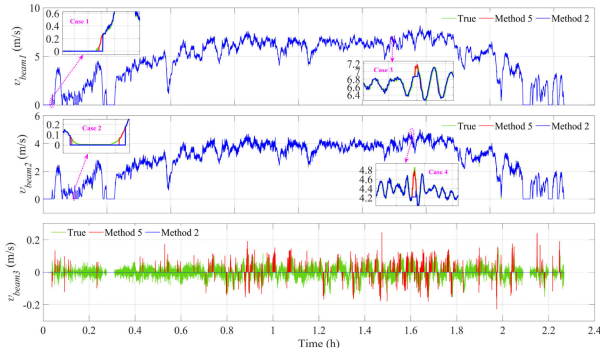
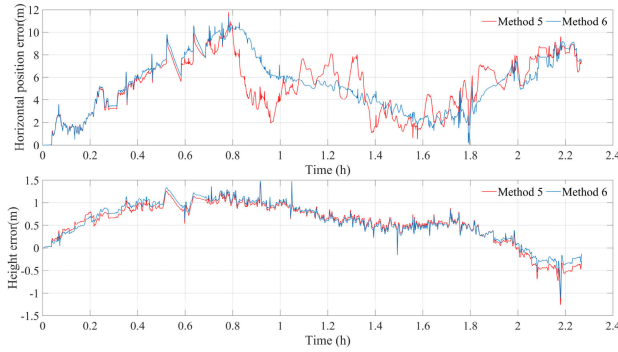Fig. 13. Filter measurement vector in Methods 2 and 5.

Fig. 14. Position error of Methods 5 and 6 in the first experiment.

The enhanced positioning accuracy of Method 3 over Method 2, and Method 5 over Method 4, suggests the importance of considering the influence of vehicle lateral velocity in integrated navigation for enhancing system accuracy. To assess the performance of the LSTM-predicted lateral velocity-assisted SINS/2D-LDV tightly coupled integration across the entire navigation process, Method 6 was introduced based on Method 5. The primary distinction between the two methods is that Method 6 utilizes the LSTM-predicted lateral velocity throughout the vehicle's entire navigation process, whereas Method 5 only employs it when a violation of the NHC lateral constraint is detected. Comparative results between Method 6 and Method 5 are shown in Fig. 14. Additionally, Fig. 15 provides a comparison between NHC-based lateral zero velocity, the LSTM-predicted lateral velocity, and the true lateral velocity obtained from high-precision SINS/GNSS integration. The results in Fig. 14 show no significant difference in positioning accuracy between Method 5 and Method 6. This is because, during normal driving without vehicle sideslip, the lateral velocity is generally very small (as shown in Fig. 15, where the lateral velocity remains close to zero most of the time). When the lateral velocity deviates from normal (i.e., when the NHC lateral constraint is violated), Method 5 can promptly detect this and replace the lateral zero velocity constraint with the predicted value. The results in Fig. 15 also indicate that the LSTM-predicted lateral velocity is very close to the true value, with significantly smaller velocity errors compared to the widely used lateral zero velocity constraint. These reduced velocity errors also lead to smoother positioning outcomes in Method 6 compared to Method 5,
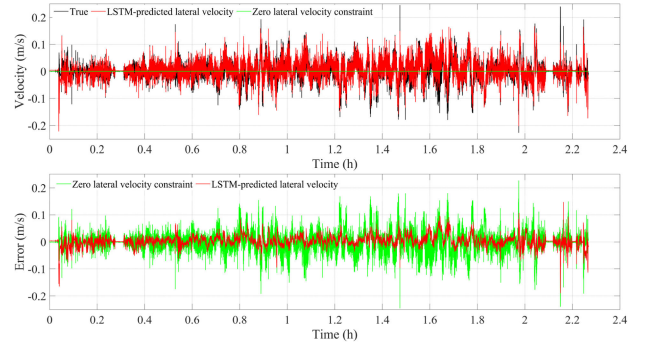

Fig. 15. Comparison of LSTM-predicted lateral velocity and zero lateral velocity constraint in the first experiment.

TABLE III
HORIZONTAL NAVIGATION PARAMETER ERRORS WITH DIFFERENT METHODS AFTER 4000 S (99.95 km)

| Methods		Horizontal position error (m)	East Velocity error (m/s)	North Velocity error (m/s)
Pure SINS	Max	520.94	0.482	0.296
	RMSE	279.01	0.154	0.144
Time updates only	Max	1797.55	4.186	0.275
	RMSE	326.05	1.063	0.126
Beam 2 failure + Method 7	Max	599.47	0.532	0.701
	RMSE	290.48	0.195	0.183
Beam 2 failure + Method 5	Max	**68.58**	**0.372**	**0.218**
	RMSE	**30.29**	**0.068**	**0.056**
Both beams failure + Method 7	Max	4411.09	3.117	2.943
	RMSE	2184.41	1.342	0.998
Both beams failure + Method 5	Max	**210.15**	**0.334**	**0.232**
	RMSE	**75.11**	**0.072**	**0.061**
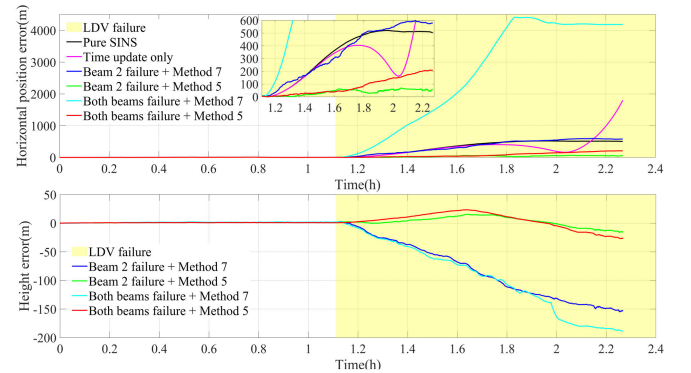
Fig. 16. Position error of the integrated navigation system in the case of 2D-LDV interruption in the first experiment.

as illustrated in Fig. 14. In conclusion, Method 5 proposed in this article is sufficient to address the impact of vehicle sideslip on integrated navigation systems in practical applications. The overall performance improvement from using LSTM-predicted lateral velocity throughout the entire vehicle navigation process is generally limited. Moreover, frequent use of the predicted lateral velocity introduces new challenges, such as increased computational demands and greater sensitivity to the accuracy of lateral velocity predictions.

In Figs. 10–13, the outliers in the LDV data were transient, typically lasting less than 3 s. Consequently, validating the
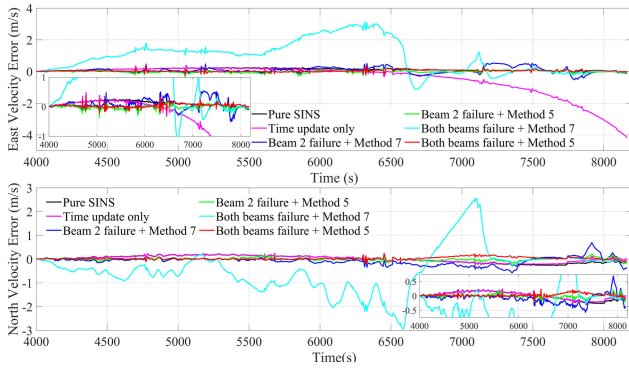
Fig. 17. Velocity error of the integrated navigation in the case of LDV interruption in the first experiment.

TABLE IV
COMPARISON OF THE PERFORMANCE OF THE FIVE METHODS IN THE SECOND EXPERIMENT (197.42 km)

Methods		RMSE (m, ‰)		Max (m, ‰)	
Method 1	Horizontal error	25.96	0.131	45.42	0.230
	Height error	8.05	0.041	17.59	0.089
Method 2	Horizontal error	21.12	0.107	37.25	0.189
	Height error	2.67	0.014	4.04	0.021
Method 3	Horizontal error	19.71	0.099	34.87	0.177
	Height error	2.67	0.014	4.06	0.021
Method 4	Horizontal error	16.98	0.086	32.63	0.165
	Height error	2.21	0.011	3.61	0.018
Method 5	Horizontal error	**16.37**	**0.083**	**30.74**	**0.156**
	Height error	**2.20**	**0.011**	**3.61**	**0.018**

Fig. 18. Vehicle trajectory in the second experiment.

Fig. 19. LDV velocity output curve in the second experiment.

robustness of the proposed method against prolonged LDV measurement interruptions becomes imperative. To thoroughly evaluate the effectiveness of the method during LDV failures, two simulations were performed using the first set of experimental data: one involving the second beam of the 2D-LDV failing at 4000 s, and another featuring a concurrent failure of both beams. In the case of LDV failure for a long period of time, Figs. 16 and 17 show the position and velocity errors using the proposed Method 5 and Method 5 without adaptive filtering (Method 7), pure inertial navigation (upward channel isolation), and navigation filter using only time updates. Table III shows the horizontal navigation parameter errors for the different methods after LDV failure (after 4000 s). The results show that during extended LDV failure (lasting 1.16 h and covering a distance of 99.95 km), the proposed method exhibited horizontal position errors RMSE of 30.29 m when a single 2D-LDV beam failed and 75.11 m when both beams failed simultaneously. Notably, the maximum height errors remained below 25 m in both cases, demonstrating the method's capability to handle long-term 2D-LDV failures. In contrast, the current SINS/LDV integration relies solely on time updates when LDV measurements fail, essentially reverting to a pure inertial navigation system. As indicated in Table III, this approach results in a maximum horizontal position error approaching 1.8 km. This divergence is attributed to the failure of the integrated navigation system to isolate the upward channel from the horizontal channel during time updates, thereby impacting horizontal positioning results. For pure SINS with isolated upward channels, the maximum horizontal position error reaches 520.94 m, which still significantly exceeds the performance of the proposed method. Thus, the proposed approach markedly improves the navigation accuracy compared to commonly used methods during prolonged 2D-LDV failures. Furthermore, the adaptive filtering method developed in this article significantly enhances integrated navigation accuracy. Using the adaptive filter, the maximum horizontal position error is decreased by 88.56% and 95.23% for single and all 2D-LDV beam failures, respectively, compared to the nonadaptive case. This underscores the importance of adjusting the prior measurement noise covariance matrix based on the prediction accuracy of the LSTM network and expanding the measurement noise

covariance matrix to mitigate outlier effects on the integrated navigation system. Moreover, the proposed method exhibits a 67.37% and 59.67% decrease in maximum horizontal position error and horizontal position RMSE, respectively, when a single 2D-LDV beam fails compared to when both beams fail simultaneously. Concurrently, it achieves improved accuracy in altitude and velocity estimation, suggesting that when one of the 2D-LDV beams fails, the remaining normal beam still effectively suppresses the navigation system errors.

To further substantiate the efficacy and assess the precision of the proposed SINS/2D-LDV integrated navigation approach, we tested it on a second set of experimental data. The movement trajectory of the vehicle and the LDV output
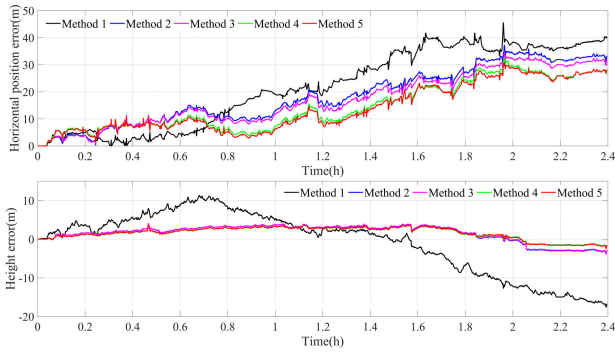
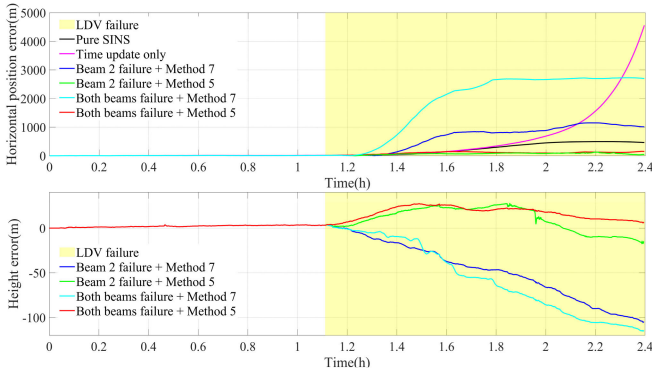Fig. 20. Position error of the second experiment.

Fig. 21. Position error of the integrated navigation system in the case of 2D-LDV interruption in the second test.

in the second experiment are depicted in Figs. 18 and 19. This experiment spanned approximately 2.39 h and covered a total distance of 197.42 km. The position errors of the different methods are depicted in Fig. 20 and Table IV. Fig. 21 shows the position errors for each method during extended periods of 2D-LDV failure. Each method's performance in the second set of experiments was similar to that in the first set. The proposed method outperforms other comparative methods both in normal use scenarios and during prolonged LDV failures, further proving its validity and superiority.

VI. CONCLUSION

To mitigate the impact of both short-term and long-term anomalies in 2D-LDV measurement value and the violation of the lateral zero-velocity constraint on the SINS/2D-LDV integration, this article proposes an LSTM-assisted SINS/2D-LDV tightly coupled integration approach using LOF and adaptive filter. Based on the SINS/2D-LDV tightly coupled approach, which directly uses the raw 2D-LDV measurement value, an LSTM network is used to predict the 2D-LDV beam measurement value and the lateral velocity of the vehicle. Concurrently, an outlier detection mechanism using LOF is constructed to identify outliers. Upon the detection of outliers, the predicted values from the LSTM network replace them. Additionally, an adaptive filter is employed to adjust the measurement noise covariance matrix to reduce the influence of predicted value errors on the navigation filter. The accuracy of the constructed measurement value prediction scheme, the validity of the designed outlier detection scheme, and the

navigation performance of the proposed method have been corroborated using data from two sets of long-distance experiments. The findings indicate that the proposed method can handle various complex scenarios and provides a new effective perspective for improving the reliability of the SINS/LDV integrated navigation system.

This research utilizes a 2D-LDV and a navigation-grade IMU within the integrated system. Subsequent research will investigate the potential of integrating SINS with 3D-LDV, as well as the feasibility of integrating LDV with low-cost SINS.

REFERENCES

[1] X. Huang, C. Yang, and M. Wen, "A sliding window filter with GNSS-state constraint for RTK-visual-inertial navigation," *IEEE Trans. Robot.*, vol. 40, pp. 1920–1937, 2024.

[2] W. Wang, W. Shangguan, J. Liu, and J. Chen, "Enhanced fault detection for GNSS/INS integration using maximum correntropy filter and local outlier factor," *IEEE Trans. Intell. Vehicles*, vol. 9, no. 1, pp. 2077–2093, Jan. 2024.

[3] S. Du, Y. Huang, B. Lin, J. Qian, and Y. Zhang, "A lie group manifold-based nonlinear estimation algorithm and its application to low-accuracy SINS/GNSS integrated navigation," *IEEE Trans. Instrum. Meas.*, vol. 71, pp. 1–27, 2022.

[4] L. Chang, Q. Bian, Y. Zuo, and Q. Zhou, "SINS/GNSS-integrated navigation based on group affine SINS mechanization in local-level frame," *IEEE/ASME Trans. Mechatronics*, vol. 28, no. 5, pp. 2471–2482, Oct. 2023.

[5] W. Ouyang, Y. Wu, and H. Chen, "INS/odometer land navigation by accurate measurement modeling and multiple-model adaptive estimation," *IEEE Trans. Aerosp. Electron. Syst.*, vol. 57, no. 1, pp. 245–262, Feb. 2021.

[6] J. Dong, X. Ren, S. Han, and S. Luo, "UAV vision aided INS/odometer integration for land vehicle autonomous navigation," *IEEE Trans. Veh. Technol.*, vol. 71, no. 5, pp. 4825–4840, May 2022.

[7] L. Han, Z. Shi, J. Song, and H. Wang, "Vehicle positioning algorithm based on NHC/virtual-MINS/OD," *IEEE Trans. Veh. Technol.*, vol. 71, no. 5, pp. 4764–4775, May 2022.

[8] J. Pan, B. Li, H. Zhang, F. Gao, X. Li, and G. Zhou, "Self-calibration of INS/odometer integrated navigation system with a large initial position error," *IEEE Sensors J.*, vol. 24, no. 7, pp. 11048–11056, Apr. 2024.

[9] A. Beauvisage, K. Ahiska, and N. Aouf, "Robust multispectral visual-inertial navigation with visual odometry failure recovery," *IEEE Trans. Intell. Transp. Syst.*, vol. 23, no. 7, pp. 9089–9101, Jul. 2022.

[10] G. He, X. Yuan, Y. Zhuang, and H. Hu, "An integrated GNSS/LiDAR-SLAM pose estimation framework for large-scale map building in partially GNSS-denied environments," *IEEE Trans. Instrum. Meas.*, vol. 70, pp. 1–9, 2021.

[11] Z. Wen, G. Yang, Q. Cai, and T. Chen, "A novel Bluetooth-odometer-aided smartphone-based vehicular navigation in satellite-denied environments," *IEEE Trans. Ind. Electron.*, vol. 70, no. 3, pp. 3136–3146, Mar. 2023.

[12] K. Kim and H. Sohn, "Dynamic displacement estimation by fusing LDV and LiDAR measurements via smoothing based Kalman filtering," *Mech. Syst. Signal Process.*, vol. 82, pp. 339–355, Jan. 2017.

[13] J. Zhou, X. Nie, and J. Lin, "A novel laser Doppler velocimeter and its integrated navigation system with strapdown inertial navigation," *Opt. Laser Technol.*, vol. 64, pp. 319–323, Dec. 2014.

[14] Q. Fu, Y. Liu, Z. Liu, S. Li, and B. Guan, "High-accuracy SINS/LDV integration for long-distance land navigation," *IEEE/ASME Trans. Mechatronics*, vol. 23, no. 6, pp. 2952–2962, Dec. 2018.

[15] M. Wang, J. Cui, Y. Huang, W. Wu, and X. Du, "Schmidt ST-EKF for autonomous land vehicle SINS/ODO/LDV integrated navigation," *IEEE Trans. Instrum. Meas.*, vol. 70, pp. 1–9, 2021.

[16] Z. Xiang, Q. Wang, R. Huang, C. Xi, X. Nie, and J. Zhou, "Position observation-based calibration method for an LDV/SINS integrated navigation system," *Appl. Opt.*, vol. 60, no. 26, p. 7869, Sep. 2021.

[17] Z. Xiang, Q. Wang, R. Huang, C. Xi, X. Nie, and J. Zhou, "In-motion initial alignment method for a laser Doppler velocimeter-aided strapdown inertial navigation system based on an adaptive unscented quaternion H-infinite filter," *Meas. Sci. Technol.*, vol. 33, no. 3, Mar. 2022, Art. no. 035001.

[18] Z. Xiang, Q. Wang, R. Huang, C. Xi, X. Nie, and J. Zhou, "A fast robust in-motion alignment method for laser Doppler velocimeter-aided strapdown inertial navigation system," *IEEE Sensors J.*, vol. 22, no. 17, pp. 17254–17265, Sep. 2022.

[19] Z. Xiang, Q. Wang, S. Jin, X. Nie, and J. Zhou, "Online calibration method for SINS/LDV integrated navigation system based on left group error definition," *Meas. Sci. Technol.*, vol. 35, no. 5, Feb. 2024, Art. no. 055106.

[20] Z. Xiang, Q. Wang, R. Huang, S. Jin, X. Nie, and J. Zhou, "A robust online calibration method for SINS/LDV integrated navigation system based on position observation," *IEEE Sensors J.*, vol. 24, no. 1, pp. 895–908, Jan. 2024.

[21] X. Nie and J. Zhou, "Pitch independent vehicle-based laser Doppler velocimeter," *Opt. Lasers Eng.*, vol. 131, Aug. 2020, Art. no. 106072.

[22] Z. Xiang et al., "A SINS/GNSS/2D-LDV integrated navigation scheme for unmanned ground vehicles," *Meas. Sci. Technol.*, vol. 34, no. 12, Dec. 2023, Art. no. 125116.

[23] Z. Xiang, Q. Wang, R. Huang, S. Jin, X. Nie, and J. Zhou, "Online calibration method for pitch-independent laser Doppler velocimeter based on improved integrated navigation model," *IEEE Trans. Instrum. Meas.*, vol. 72, pp. 1–13, 2023.

[24] X. Zhang, Y. Zhou, F. Zhu, and H. Hu, "A new vehicle motion constraint model with parameter autonomous learning and analysis on inertial drift error suppression," *Acta Geodaetica et Cartographica Sinica*, vol. 51, no. 7, p. 1249, Aug. 2022.

[25] W. Liu, Q. Nong, X. Tao, F. Zhu, and J. Hu, "OD/SINS adaptive integrated navigation method with non-holonomic constraints," *Acta Geodaetica et Cartographica Sinica*, vol. 51, no. 1, p. 9, 2022.

[26] M. Brossard, A. Barrau, and S. Bonnabel, "AI-IMU dead-reckoning," *IEEE Trans. Intell. Vehicles*, vol. 5, no. 4, pp. 585–595, Dec. 2020.

[27] X. Li, H. Li, G. Huang, Q. Zhang, and S. Meng, "Non-holonomic constraint (NHC)-assisted GNSS/SINS positioning using a vehicle motion state classification (VMSC)-based convolution neural network," *GPS Solutions*, vol. 27, no. 3, p. 144, Jun. 2023.

[28] Y. Xu, K. Wang, C. Yang, Z. Li, F. Zhou, and D. Liu, "GNSS/INS/OD/NHC adaptive integrated navigation method considering the vehicle motion state," *IEEE Sensors J.*, vol. 23, no. 12, pp. 13511–13523, Jun. 2023.

[29] Y. Huang, Y. Zhang, B. Xu, Z. Wu, and J. A. Chambers, "A new adaptive extended Kalman filter for cooperative localization," *IEEE Trans. Aerosp. Electron. Syst.*, vol. 54, no. 1, pp. 353–368, Feb. 2018.

[30] Y. Jiang, P. Ma, and H. Baoyin, "Residual-normalized strong tracking filter for tracking a noncooperative maneuvering spacecraft," *J. Guid., Control, Dyn.*, vol. 42, no. 10, pp. 2304–2309, Oct. 2019.

[31] L. Wang, X. Niu, T. Zhang, H. Tang, and Q. Chen, "Accuracy and robustness of ODO/NHC measurement models for wheeled robot positioning," *Measurement*, vol. 201, Sep. 2022, Art. no. 111720.

[32] Y. Wu, X. Niu, and J. Kuang, "A comparison of three measurement models for the wheel-mounted MEMS IMU-based dead reckoning system," *IEEE Trans. Veh. Technol.*, vol. 70, no. 11, pp. 11193–11203, Nov. 2021.

[33] W. Fang et al., "A LSTM algorithm estimating pseudo measurements for aiding INS during GNSS signal outages," *Remote Sens.*, vol. 12, no. 2, p. 256, Jan. 2020.

[34] H. Tang, X. Niu, T. Zhang, Y. Li, and J. Liu, "OdoNet: Untethered speed aiding for vehicle navigation without hardware wheeled odometer," *IEEE Sensors J.*, vol. 22, no. 12, pp. 12197–12208, Jun. 2022.

[35] J. Zhu, A. Li, F. Qin, L. Chang, and L. Qian, "A hybrid method for dealing with DVL faults of SINS/DVL integrated navigation system," *IEEE Sensors J.*, vol. 22, no. 16, pp. 15844–15854, Aug. 2022.

[36] Y. Yao, X. Xu, X. Xu, and I. Klein, "Virtual beam aided SINS/DVL tightly coupled integration method with partial DVL measurements," *IEEE Trans. Veh. Technol.*, vol. 72, no. 1, pp. 418–427, Jan. 2023.

[37] X. Meng, H. Tan, P. Yan, Q. Zheng, G. Chen, and J. Jiang, "A GNSS/INS integrated navigation compensation method based on CNN–GRU + IRAKF hybrid model during gnss outages," *IEEE Trans. Instrum. Meas.*, vol. 73, 2024, Art. no. 2510015.

[38] Y. Qin, *Inertial Navigation*, 3rd ed. Beijing, China: China Science Press, 2020.

[39] X. Shi, Z. Chen, H. Wang, D.-Y. Yeung, W.-K. Wong, and W. Woo, "Convolutional LSTM network: A machine learning approach for precipitation nowcasting," in *Proc. Adv. Neural Inf. Process. Syst.*, vol. 28, 2015, pp. 1–9.

[40] R. A. Horn and C. R. Johnson, *Matrix Analysis*. Cambridge, U.K.: Cambridge Univ. Press, 2012.

[41] F. Si, Y. Han, J. Wang, and Q. Zhao, "Connectivity verification in distribution systems using smart meter voltage analytics: A cloud-edge collaboration approach," *IEEE Trans. Ind. Informat.*, vol. 17, no. 6, pp. 3929–3939, Jun. 2021.

[42] Q. Xie, G. Tao, C. Xie, and Z. Wen, "Abnormal data detection based on adaptive sliding window and weighted multiscale local outlier factor for machinery health monitoring," *IEEE Trans. Ind. Electron.*, vol. 70, no. 11, pp. 11725–11734, Nov. 2023.

[43] M. M. Breunig, H.-P. Kriegel, R. T. Ng, and J. Sander, "LOF: Identifying density-based local outliers," in *Proc. ACM SIGMOD Int. Conf. Manage. Data*, Dallas, TX, USA, May 2000, pp. 93–104.

[44] D. P. Kingma and J. Ba, "Adam: A method for stochastic optimization," 2014, *arXiv:1412.6980*.

[45] L. Qian, F. Qin, A. Li, K. Li, and J. Zhu, "An INS/DVL integrated navigation filtering method against complex underwater environment," *Ocean Eng.*, vol. 278, Jun. 2023, Art. no. 114398.

Zhiyi Xiang received the M.E. degree from the College of Advanced Interdisciplinary Studies, National University of Defense Technology, Changsha, China, in 2021, where he is currently pursuing the Ph.D. degree.

His current research interests include SINS/LDV integrated navigation technology.

Qi Wang received the M.E. degree from the College of Optoelectronic Science and Engineering, National University of Defense Technology, Changsha, China, in 2013, and the Ph.D. degree from the College of Advanced Interdisciplinary Studies, National University of Defense Technology, in 2018.

He is currently an Associate Professor with the College of Advanced Interdisciplinary Studies, National University of Defense Technology. His research interests include laser Doppler velocimetry and SINS/LDV integrated navigation technology.

Xiaoming Nie received the M.E. and Ph.D. degrees from the College of Optoelectronic Science and Engineering, National University of Defense Technology, Changsha, China, in 2010 and 2014, respectively.

He is currently an Associate Professor with the College of Advanced Interdisciplinary Studies, National University of Defense Technology. His research interests include optoelectronic velocimetry, laser Doppler velocimetry, and SINS/LDV integrated navigation technology.

Shilong Jin received the M.E. and Ph.D. degrees from the College of Optoelectronic Science and Engineering, National University of Defense Technology, Changsha, China, in 1994 and 2006, respectively.

He is currently a Professor with the College of Advanced Interdisciplinary Studies, National University of Defense Technology. His research interests include optoelectronic detection technology and inertial sensors and systems.

Jian Zhou received the B.E. and Ph.D. degrees from the College of Optoelectronic Science and Engineering, National University of Defense Technology, Changsha, China, in 2006 and 2011, respectively.

He is currently an Associate Professor with the College of Advanced Interdisciplinary Studies, National University of Defense Technology. His research interests include optoelectronic velocimetry, laser Doppler velocimetry, and SINS/LDV integrated navigation technology.